amcs

AN UNSCENTED TRANSFORMATION APPROACH TO STOCHASTIC ANALYSIS OF MEASUREMENT UNCERTAINTY IN MAGNET RESONANCE IMAGING WITH APPLICATIONS IN ENGINEERING

ANDREAS RAUH [a], KRISTINE JOHN [b], CAROLIN WÜSTENHAGEN [b],
MARTIN BRUSCHEWSKI [b,*], SVEN GRUNDMANN [b]

[a]Lab-STICC
ENSTA Bretagne
2 rue François Verny, 29806 Brest, France
e-mail: Andreas.Rauh@interval-methods.de

[b]Institute of Fluid Mechanics
University of Rostock
Justus-von-Liebig-Weg 2, D-18059 Rostock, Germany
e-mail: {Kristine.John,Carolin.Wuestenhagen}@uni-rostock.de,
{Martin.Bruschewski,Sven.Grundmann}@uni-rostock.de

In the frame of stochastic filtering for nonlinear (discrete-time) dynamic systems, the unscented transformation plays a vital role in predicting state information from one time step to another and correcting *a priori* knowledge of uncertain state estimates by available measured data corrupted by random noise. In contrast to linearization-based techniques, such as the extended Kalman filter, the use of an unscented transformation not only allows an approximation of a nonlinear process or measurement model in terms of a first-order Taylor series expansion at a single operating point, but it also leads to an enhanced quantification of the first two moments of a stochastic probability distribution by a large signal-like sampling of the state space at the so-called sigma points which are chosen in a deterministic manner. In this paper, a novel application of the unscented transformation technique is presented for the stochastic analysis of measurement uncertainty in magnet resonance imaging (MRI). A representative benchmark scenario from the field of velocimetry for engineering applications which is based on measured data gathered at an MRI scanner concludes this contribution.

Keywords: magnet resonance imaging, compressed sensing, stochastic uncertainty, unscented transformation.

1. Introduction

Although MRI techniques are widely associated with medical examinations, they have gained a significant amount of interest also in various engineering disciplines such as fluid mechanics. This fact mostly stems from the possibility of gathering spatially multi-dimensional insight into complex (opaque) structures without requiring optical or physical access as most conventional measurements do (e.g., by applying laser-optical techniques). Engineering applications of MRI, for example, in fluid mechanics, include the quantification of the mean velocities and temperature fields in complex flow systems, which could not be obtained with any other measurement technique (Bruschewski *et al.*, 2019). As the fundamental principle of these MRI techniques, the measured information is encoded in the phase angle values of the reconstructed image.

Possible applications in this context were reported for the optimization of fluidic components, such as fuel injection systems for combustion engines, internal cooling for turbine blades, or various types of heat exchangers (Elkins and Alley, 2007). The fact that the use of MRI simplifies the investigation of such opaque structures also opens up a wide range of

---

*Corresponding author

future applications in the field of control, especially for experimental validation of simplified dynamic models for complex thermo-fluidic systems. In such cases, the admissibility of the replacement of complex, commonly nonlinear, models consisting of coupled partial differential equations for heat and mass transfer has to be validated. This replacement is possible if sufficiently accurate formulations can be found in terms of lumped-parameter, reduced-order models, which are typically derived by finite volume, finite difference, or finite element approaches (Rauh *et al.*, 2011; Kostin *et al.*, 2014). As such, MRI results may help in optimizing future control scenarios, where a trade-off between high modeling accuracy and a minimum amount of numerical effort is required.

It is especially in the engineering applications mentioned above that reliable quantitative data are required. Therefore, it is essential to quantify the effect of measurement uncertainty that is ubiquitous due to the thermal noise of the receiver chain. As shown by Bruschewski *et al.* (2016), this noise can be characterized with good accuracy by a Gaussian probability density (Gaussian PDF) for each measured data point if the variance between two equally measured images is determined. The influence of these measurement uncertainties is even more pronounced if advanced measurement techniques are applied, which require iterative image reconstruction (Zhou *et al.*, 2020).

These reconstruction methods generally become necessary if the data acquisition in MRI is undersampled to allow a significant acceleration of the data acquisition. This enables, for example, time-resolved measurements (Niebergall *et al.*, 2013) or acceleration of high accuracy measurements (John *et al.*, 2020a). However, iterative approaches suffer from reconstruction artifacts which may lead to the so-called *staircase* effect. This effect becomes especially pronounced if the aforementioned undersampling techniques are employed. Qualitatively speaking, the staircase effect leads to the phenomenon that some regions in the reconstructed image turn into virtually constant ones. Hence, it is essential to find relations between this undesirable effect and stochastically distributed measurement errors to develop algorithms in future work which will counter those phenomena.

Our previous work has dealt with a first approach to quantify the effect of measurement uncertainty by representing the possible ranges of consistently reconstructed data in MRI-based signal processing with the help of purely set-valued, non-probabilistic approaches. John *et al.* (2020b) and Rauh *et al.* (2020) showed that interval analysis (as a set-valued approach) provides a helpful tool to detect those domains in the reconstructed images that are influenced most by the assumed *bounded* measurement uncertainty.

Quantification of these effects became possible with the help of computing the *worst-case deviations* between the estimated suprema and infima of reconstructed phase angles.

However, a fundamental drawback of the use of interval analysis is its property to *overestimate* the resulting domains in a conservative manner. Moreover, interval analysis does not provide any information regarding the *probability distribution* of reconstructed data within the computed bounds. Before tackling this latter issue by employing a combination of interval analysis with the notion of fuzzy sets or type-2 interval arithmetic in future research, as suggested by Măceş and Stadtherr (2013) or Piegat and Dobryakova (2020), to predict certain confidence intervals or uncertainty in interval bounds, a purely stochastic analysis of measurement errors is performed in this paper. As shown in the following sections, the aforementioned iterative image reconstruction is characterized by nonlinear least-squares optimization that can be cast into an iterative solution of the corresponding necessary optimality conditions.

Previously, the evaluation of these conditions was performed with the help of interval analysis. However, those interval approaches require application-specific insight concerning the derivation of meaningful bounds for the expected measurement errors. As discussed by John *et al.* (2020b) and Rauh *et al.* (2020), suitable options for such models are the assumption of independent additive bounds for each measured point in the frequency domain or uncertainty models that are related to the power spectral density of the acquired data. The validity of such assumptions, however, needs to be checked for each measurement scenario. In contrast, the use of uncertainty models relying on Gaussian PDFs (mainly focusing on the thermal noise in the MRI receiver chain) is application-independent and therefore in the focus of this paper.

To quantify the stochastic distribution of measurement errors in all signal processing stages, an unscented transformation[1] approach, well known from the prediction stage of nonlinear discrete-time filtering procedures (cf. the unscented Kalman filter developed originally by Julier *et al.* (2000)), is proposed in this paper to solve the corresponding identification task. Due to the use of the so-called sigma points (which are generated in a deterministic way despite the probabilistic nature of the measurement process), the first two moments of the probability distribution of the

---

[1]This kind of transform represents a mathematical function that allows estimating the stochastic moments resulting from some nonlinear mapping in terms of a finite number of input arguments. Most commonly, it is employed to estimate the mean and covariance in nonlinear filtering. The notion of an *unscented* transformation, however, is a more or less arbitrary name that was introduced by its developer, J. Uhlmann, to avoid referring to his own name (Uhlmann, 2021).

reconstructed image can be characterized accurately despite nonlinearities. Using sigma points avoids the often tedious and time-consuming evaluation of Jacobian matrices of large dimensions, which a first-order Taylor series linearization would require. Besides, the unscented transformation commonly enhances state estimates in comparison with a pure first-order linearization and often represents a computationally efficient alternative to brute force Monte-Carlo sampling or particle filtering.

Section 2 of this paper provides a summary of the nonlinear least-squares optimization task that is typically solved if compressed sensing techniques in the frame of MRI are considered. As mentioned above, this optimization problem is cast into the iterative solution of a nonlinear set of algebraic equations. In this paper, a strict proof of convergence of this iteration is provided by proving the Lipschitz continuity of the respective contracting map. Section 3 focuses on the unscented transformation allowing quantifying the uncertainty of the reconstructed images, which permits one to predict the first two moments of the PDF reliably. In addition, the distribution of the sigma points provides further insight into possible multi-modality and higher moments of the PDF for low-dimensional characteristics deduced from the image reconstruction, such as flow rates or mean temperatures in the case of velocity-encoded or temperature-encoded measurements. Details on numerical results, including a comparison between a standard CPU implementation and the use of the GPU (Datta *et al.*, 2019) to massively parallelize the required multiplication of large matrices, are given in Section 4. The data employed for the numerical validation were measured at the MRI Flow Lab, which is part of the Institute of Fluid Mechanics at the University of Rostock, Germany. Finally, conclusions and an outlook on future work with a focus on interfacing set-valued with probabilistic evaluation techniques are given in Section 5.

2. Least-squares estimation techniques for compressed sensing in the frame of MRI

An acceleration of MRI measurements becomes possible with the use of so-called *compressed sensing* (Holland *et al.*, 2010; Zhao *et al.*, 2012; Zhao, 2014). This method relies on the fact that information in the frame of MRI has a sparse representation in a known transformation domain. In compressed sensing, undersampling enables a strong acceleration of the measurement. This undersampling is performed randomly to avoid coherent aliasing artifacts. The unmeasured data are set to zero.

MRI measurement data (denoted by the complex-valued matrix $\mathbf{Y} \in \mathbb{C}^{m \times n}$ throughout this paper) consist of spatial frequencies. If the frequency range were fully sampled, the inverse multi-dimensional discrete Fourier transformation (DFT) would enable the

transformation of the data into the spatial domain. As a linear operator, the (inverse) DFT is characterized by the fact that Gaussian noise in the frequency domain results in perfectly Gaussian uncertainty in the reconstructed image. It is assumed that this property is lost due to additional uncertainty resulting from undersampling which can partially be traced back to the staircase effect described by Zhou *et al.* (2020), as well as due to nonlinear operations applied to the reconstructed data set $\mathbf{X} \in \mathbb{C}^{m \times n}$ in further signal processing stages. For the sake of the compact notation of the following mathematical problem formulation, the operators $\mathbf{x} = \text{col}(\mathbf{X}) \in \mathbb{C}^{m \cdot n}$ and $\mathbf{y} = \text{col}(\mathbf{Y}) \in \mathbb{C}^{m \cdot n}$ are further employed, which turn the matrices $\mathbf{X}$ and $\mathbf{Y}$ into stacked column vectors in a column-wise form.

Within this paper, the loss of the property of Gaussian probability distributions is confirmed by the mapping of specific sigma points in Sections 3 and 4 into frequency distributions with a non-Gaussian shape.

Randomly undersampling the data $\mathbf{Y}$ leads to additional noise-like artifacts. These are reduced with the help of an iterative nonlinear image reconstruction, where sparsity is enforced by means of regularization terms that involve finite difference and Wavelet operators applied to the reconstructed image $\mathbf{X}$. As discussed by John *et al.* (2020b), most state-of-the-art techniques for this reconstruction make use of classical floating-point optimization techniques (for example, complex-valued conjugate gradient approaches or variants of Gauss–Newton methods) (Holland *et al.*, 2010; Tamir *et al.*, 2016). However, drawbacks of such numerical solvers are an increase in the computing times for signal processing and the lack of possibilities for direct quantification of the influence of measurement uncertainty in the data $\mathbf{Y}$ unless multiple image reconstructions are performed in a Monte-Carlo like manner. Unfortunately, such approaches rapidly turn into excessively time-consuming tasks. A significant reduction of computing times, as well as enhanced possibilities for an algorithmic parallelization, are obtained by the iteration procedure derived in the following.

2.1. Specification of the cost function for an iterative image reconstruction. In previous work, we focused on a first attempt to quantify the influence of uncertainty during the minimization of the cost function

$$J(\mathbf{x}) = Q_1(\mathbf{x}) + \lambda_1 \cdot Q_{\text{TV}}(\mathbf{x}) \\ + \lambda_2 \cdot Q_{\text{W}}(\mathbf{x}) + \lambda_3 \cdot Q_{\text{Mb}}(\mathbf{x}) \tag{1}$$

by means of an interval-based iteration scheme in the set-valued context mentioned in Introduction (cf. Rauh *et al.*, 2020). The cost function (1) consists of the following four individual summands:

- $Q_1(\mathbf{x})$ as the fundamental requirement for consistency between the measured data $\mathbf{Y}$ and the reconstructed image $\mathbf{X}$ (which are interconnected in terms of the multi-dimensional DFT),

- $Q_{\mathrm{TV}}(\mathbf{x})$ and $Q_{\mathrm{W}}(\mathbf{x})$ as two penalty terms that enforce the aforementioned property of sparsity, and

- $Q_{\mathrm{Mb}}(\mathbf{x})$ for windowing out data outside a certain domain of investigation.

The consistency between $\mathbf{Y}$ and $\mathbf{X}$ in $Q_1(\mathbf{x})$ restricts the global minimum to be in accordance with the measured data, whereas the constituents $Q_{\mathrm{TV}}(\mathbf{x})$ and $Q_{\mathrm{W}}(\mathbf{x})$ of (1) restrict the solution under the assumption that the MRI image has a sparse representation in a known transform domain if noise and undersampling artifacts are eliminated. Therefore, they enforce the sparsity of the solution. Finally, as noise and undersampling artifacts lead to non-zero background signal intensities, $Q_{\mathrm{Mb}}(\mathbf{x})$ aims at forcing them to zero. Note that $Q_{\mathrm{Mb}}(\mathbf{x})$ can only be applied when the geometry of the measured object is well known, such as in engineering applications.

According to the state-of-the-art in signal processing for MRI (cf. Holland *et al.*, 2010; Tamir *et al.*, 2016; Zhou *et al.*, 2020), the data consistency requirement is expressed as the quadratic norm[2]

$$\begin{aligned} Q_1(\mathbf{x}) &= \left\| \tilde{\mathbf{M}}_{\mathrm{s}} \circ \mathcal{F}^{\langle 2 \rangle} \{\mathbf{X}\} - \mathbf{Y} \right\|_2^2 \\ &= \left(\boldsymbol{\mathcal{M}}_{\mathrm{s}} \cdot \mathbf{x} - \mathbf{y}' \right)^H \cdot \left(\boldsymbol{\mathcal{M}}_{\mathrm{s}} \cdot \mathbf{x} - \mathbf{y}' \right) , \end{aligned} \quad (2)$$

where the vector $\mathbf{y}' \in \mathbb{C}^{N'}$, $N' \leq m \cdot n$, is a sub-vector of the measurement reshaped into the column-wise notation $\mathbf{y} = \mathrm{col}(\mathbf{Y})$ after removing all zero elements.

In addition, the matrix $\tilde{\mathbf{M}}_{\mathrm{s}}$ (representing undersampling and zero-filling) is connected by the element-wise Hadamard product with the two-dimensional (2D) DFT

$$\mathcal{F}^{\langle 2 \rangle} \{\mathbf{X}\} = \mathcal{F} \left\{ \mathcal{F} \{\mathbf{X}\}^T \right\}^T. \quad (3)$$

In the second line of (2), this connection is alternatively expressed by

$$\boldsymbol{\mathcal{M}}_{\mathrm{s}} = \mathbf{M}_{\mathrm{s}} \cdot \left(\mathbf{W}_2 \otimes \mathbf{W}_1 \right), \quad (4)$$

where $\mathbf{M}_{\mathrm{s}}$ is the counterpart of $\tilde{\mathbf{M}}_{\mathrm{s}}$ in a classical matrix product notation.

The relation (4) is based on a column-wise notation

$$\begin{aligned} \mathrm{col}\left(\mathcal{F}^{\langle 2 \rangle} \{\mathbf{X}\} \right) &= \mathrm{col}\left(\mathbf{W}_1 \cdot \mathbf{X} \cdot \mathbf{W}_2^T \right) \\ &= \left(\mathbf{W}_2 \otimes \mathbf{W}_1 \right) \cdot \mathbf{x} \end{aligned} \quad (5)$$

of the 2D-DFT. It is obtained in a straightforward way by formulating the 2D-DFT in terms of a complex-valued matrix product (cf. Rao and Yip, 2000; Gentleman, 1968; Theilheimer, 1969; Proakis and Manolakis, 1996), and subsequently applying fundamental rules for Kronecker matrix products (Weinmann, 1991) after reshaping the matrix $\mathbf{X}$ into its equivalent column vector form $\mathbf{x} = \mathrm{col}(\mathbf{X}) \in \mathbb{C}^{m \cdot n}$. In (4) and (5), the matrices

$$\mathbf{W}_1 = \mathcal{F}\{\mathbf{I}_m\} \quad \text{and} \quad \mathbf{W}_2 = \mathcal{F}\{\mathbf{I}_n\} \quad (6)$$

result form a column-wise application of the normalized 1D-DFT operator to the square identity matrices $\mathbf{I}_m \in \mathbb{R}^{m \times m}$ and $\mathbf{I}_n \in \mathbb{R}^{n \times n}$; the normalization of the DFT yields their inverses in terms of

$$\mathbf{W}_1^{-1} = \mathbf{W}_1^H \quad \text{and} \quad \mathbf{W}_2^{-1} = \mathbf{W}_2^H \quad (7)$$

due to the unitarity of the respective matrices.

The next two terms $Q_{\mathrm{TV}}(\mathbf{x})$ and $Q_{\mathrm{W}}(\mathbf{x})$ of (1) are given as the sparsity-enforcing finite difference[3] and wavelet transform operators TV and W as suggested by Holland *et al.* (2010). To ensure global differentiability of these terms for the following algorithmic steps, these operators are accounted for by the square root approximations

$$Q_\iota(\mathbf{x}) = \sqrt{ \|\boldsymbol{\Psi}_\iota \cdot \mathbf{x}\|_2^2 + \mu_\iota }, \quad \iota \in \{\mathrm{TV}, \mathrm{W}\}, \quad (8)$$

representing a regularized version of the usually applied 1-norms (John *et al.*, 2020b) with the sufficiently small parameters $\mu_\iota > 0$, $\iota \in \{\mathrm{TV}, \mathrm{W}\}$.

As described in detail by John *et al.* (2020b), the two-dimensional finite difference operator $Q_{\mathrm{TV}}(\mathbf{x})$ can be expressed with the help of

$$\boldsymbol{\Psi}_{\mathrm{TV}} := \left(\mathbf{I}_n \otimes \mathbf{T}_m \right) + \left(\mathbf{T}_n \otimes \mathbf{I}_m \right) = \boldsymbol{\Psi}_{\mathrm{TV}}^* , \quad (9)$$

where the matrices

$$\mathbf{T}_\xi = \begin{bmatrix} \mathbf{B}_{\xi-1}(-1, 1) & \mathbf{e}_{\xi-1} \\ \mathbf{0}_{\xi-1}^T & 0 \end{bmatrix} \quad \text{for } \xi \in \{m, n\} \quad (10)$$

are constructed by the $(\xi - 1)$-th unit vector $\mathbf{e}_{\xi-1} \in \mathbb{R}^{\xi-1}$, in which all elements are zero except for the entry in the position $\xi - 1$, which is equal to one, the zero vector $\mathbf{0}_{\xi-1}$ of dimension $\xi - 1$, and the upper bi-diagonal

---

[2]Throughout the paper, $(\cdot)^*$ represents the complex conjugate of the given argument and $(\cdot)^H = \left((\cdot)^*\right)^T$ is the conjugate transpose of a vector or matrix.

[3]Without loss of generality concerning the presented unscented transformation approach for uncertainty quantification, we restrict ourselves to a first-order finite-difference scheme for the TV transform operator. However, extensions towards finite-difference approximations of second-order spatial derivatives as proposed by Zhou *et al.* (2020) for a reduction in the staircase effect can be introduced analogously in future work by a generalization of (8) and (9).

Toeplitz matrix

$$\mathbf{B}_\xi(a,b) = \begin{bmatrix} a & b & 0 & \cdots & 0 \\ 0 & a & b & \ddots & \vdots \\ \vdots & \ddots & \ddots & \ddots & 0 \\ & & \ddots & a & b \\ 0 & \cdots & & 0 & a \end{bmatrix} \in \mathbb{R}^{\xi \times \xi}. \quad (11)$$

Note, in a similar fashion, also the general Wavelet transformation operator $Q_W(\mathbf{x})$ can be restated in dependence of the complex-valued matrix-vector product $\boldsymbol{\Psi}_W \cdot \mathbf{x}$, (cf. John *et al.*, 2020b).

The final term

$$Q_{\mathrm{Mb}}(\mathbf{x}) = \left\| (\mathbf{I} - \mathbf{M}_\mathrm{b}) \circ \mathbf{X} \right\|_2^2$$
$$= \mathbf{x}^H \cdot \mathrm{diag}\left\{ \mathrm{col}(\mathbf{I} - \mathbf{M}_\mathrm{b}) \right\} \cdot \mathbf{x} \quad (12)$$
$$=: \mathbf{x}^H \cdot \boldsymbol{\mathcal{M}}_\mathrm{b} \cdot \mathbf{x}$$

of the cost function (1) contains a binary mask $\mathbf{M}_\mathrm{b}$ with which all points in the image $\mathbf{X}$ are set to zero at which no relevant measurement signals exist (for example, tube walls or the outside area of a liquid-filled tube). In all following stages, the weighting factors $\lambda_1, \lambda_2, \lambda_3$ in (1) are assumed to be given as strictly nonnegative values that are fixed prior to the minimization of the cost function (1).

2.2. Necessary optimality criterion.

Theorem 1. (Necessary optimality criterion) *The necessary optimality condition for the iterative image reconstruction is given by the nonlinear, implicit algebraic equation*

$$\boldsymbol{\mathcal{N}}_{\mathrm{sb}} \cdot \mathbf{x} = \boldsymbol{\mathcal{M}}_\mathrm{s}^H \cdot \mathbf{y}' - \left(\lambda_1 \cdot \mathbf{f}_{\mathrm{TV}}(\mathbf{x}) + \lambda_2 \cdot \mathbf{f}_W(\mathbf{x}) \right) \quad (13)$$

with

$$\boldsymbol{\mathcal{N}}_{\mathrm{sb}} := \boldsymbol{\mathcal{M}}_\mathrm{s}^H \cdot \boldsymbol{\mathcal{M}}_\mathrm{s} + \lambda_3 \cdot \boldsymbol{\mathcal{M}}_\mathrm{b} \quad (14)$$

to be solved for the vector $\mathbf{x} \in \mathbb{C}^{m \cdot n}$.

Proof. By differentiating the cost function $J(\mathbf{x})$ defined in (1) independently with respect to the vectors $\mathbf{x}$ and $\mathbf{x}^*$ according to the rules for the complex-valued Wirtinger derivative (Bouboulis, 2010; Hörmander, 1990)—see John *et al.* (2020b), the equality

$$\frac{\partial J(\mathbf{x})}{\partial \mathbf{x}^*} = \left(\frac{\partial J(\mathbf{x})}{\partial \mathbf{x}} \right)^* \quad (15)$$

is obtained. It can be shown that both the left- and right-hand side of (15) provide the same necessary optimality condition (in terms of a regular unconstrained minimum) according to

$$\mathbf{f}(\mathbf{x}) = \frac{\partial J(\mathbf{x})}{\partial \mathbf{x}^*}$$
$$= \mathbf{f}_1(\mathbf{x}) + \lambda_1 \cdot \mathbf{f}_{\mathrm{TV}}(\mathbf{x}) \quad (16)$$
$$+ \lambda_2 \cdot \mathbf{f}_W(\mathbf{x}) + \lambda_3 \cdot \mathbf{f}_{\mathrm{Mb}}(\mathbf{x}) = \mathbf{0}$$

with the individual terms

$$\mathbf{f}_1(\mathbf{x}) := \frac{\partial Q_1(\mathbf{x})}{\partial \mathbf{x}^*}$$
$$= \boldsymbol{\mathcal{M}}_\mathrm{s}^H \cdot (\boldsymbol{\mathcal{M}}_\mathrm{s} \cdot \mathbf{x} - \mathbf{y}'), \quad (17)$$
$$\mathbf{f}_\iota(\mathbf{x}) := \frac{\partial Q_\iota(\mathbf{x})}{\partial \mathbf{x}^*}$$
$$= \frac{\boldsymbol{\Psi}_\iota^{*T} \cdot \boldsymbol{\Psi}_\iota \cdot \mathbf{x}}{2 Q_\iota(\mathbf{x})}, \quad \iota \in \{\mathrm{TV}, \mathrm{W}\},$$
$$(18)$$

and

$$\mathbf{f}_{\mathrm{Mb}}(\mathbf{x}) := \frac{\partial Q_{\mathrm{Mb}}(\mathbf{x})}{\partial \mathbf{x}^*} = \boldsymbol{\mathcal{M}}_\mathrm{b} \cdot \mathbf{x}. \quad (19)$$

Separating the linear dependency on $\mathbf{x}$ from all nonlinear terms completes the proof. ∎

Remark 1. The nonlinearity on the right-hand side of (16) is the reason why there exist no analytic results for the optimal solution, except for the case of $\lambda_1 = \lambda_2 = 0$. The latter case is used in the following subsection to initialize a converging fixed-point iteration as a solution to the necessary optimality conditions.

2.3. Iterative solution approach.

Theorem 2. (Fixed point-based image reconstruction) *Assuming dominance of the data consistency term $Q_1(\mathbf{x})$ with sufficiently small non-negative values of $\lambda_1 \ll 1$ and $\lambda_2 \ll 1$, a converging fixed-point iteration for the solution of the necessary optimality condition according to Theorem 1 is given by*

$$\mathbf{x}^{\langle \kappa + 1 \rangle} = \mathbf{F}(\mathbf{y}', \mathbf{x}^{\langle \kappa \rangle})$$
$$:= \mathbb{M}_{\mathrm{sb}} \cdot \boldsymbol{\mathcal{M}}_\mathrm{s}^H \cdot \mathbf{y}' \quad (20)$$
$$- \mathbb{M}_{\mathrm{sb}} \cdot \left(\lambda_1 \cdot \mathbf{f}_{\mathrm{TV}}(\mathbf{x}^{\langle \kappa \rangle}) + \lambda_2 \cdot \mathbf{f}_W(\mathbf{x}^{\langle \kappa \rangle}) \right)$$

with

$$\mathbf{x}^{\langle 0 \rangle} = \mathbb{M}_{\mathrm{sb}} \cdot \boldsymbol{\mathcal{M}}_\mathrm{s}^H \cdot \mathbf{y}'. \quad (21)$$

Proof. Pre-multiplication of (16) by $\boldsymbol{\mathcal{N}}_{\mathrm{sb}}^{-1}$, approximated by means of

$$\boldsymbol{\mathcal{N}}_{\mathrm{sb}}^{-1} \approx \mathbb{M}_{\mathrm{sb}} := 2\mathbf{I}_{m \cdot n} - \boldsymbol{\mathcal{N}}_{\mathrm{sb}} \quad (22)$$

leads to the formulation given in (20), where all nonlinear terms are evaluated for the vector $\mathbf{x}^{\langle \kappa \rangle}$ of the previous iteration step. The approximation of the matrix inverse in (22) results from a straightforward truncation of the Neumann series

$$(\mathbf{I} - \mathbf{T})^{-1} = \sum_{k=0}^{\infty} \mathbf{T}^k \quad (23)$$

after its linear term. As shown by John *et al.* (2020b), this approximation avoids numerical problems of finding the exact matrix inverse $\mathcal{N}_{\text{sb}}^{-1}$ of dimension $(m \cdot n) \times (m \cdot n)$ and converges as $\|\mathbf{T}^k\| < 1$ is satisfied for some $k \geq 1$.

The iteration in Theorem 2 converges, since

$$\left\|\mathbf{F}(\mathbf{y}', \mathbf{x}_{\text{A}}) - \mathbf{F}(\mathbf{y}', \mathbf{x}_{\text{B}})\right\| \leq L \cdot \|\mathbf{x}_{\text{A}} - \mathbf{x}_{\text{B}}\| \quad (24)$$

holds with the Lipschitz constant $L < 1$ for two arbitrary complex-valued arguments $\mathbf{x}_{\text{A}}$ and $\mathbf{x}_{\text{B}}$.

An upper bound $\overline{L} \geq L$ for this Lipschitz constant can be computed by

$$
\begin{aligned}
L &\leq \sup_{\mathbf{x} \in \mathbb{C}^{m \cdot n}} \left\{ \left\| \frac{\partial \mathbf{F}(\mathbf{y}', \mathbf{x})}{\partial \mathbf{x}} \right\| \right\} \\
&= \sup_{\mathbf{x} \in \mathbb{C}^{m \cdot n}} \left\{ \left\| \mathbb{M}_{\text{sb}} \cdot \left(\lambda_1 \cdot \mathbf{H}_{\text{TV}}(\mathbf{x}) + \lambda_2 \cdot \mathbf{H}_{\text{W}}(\mathbf{x}) \right) \right\| \right\} \\
&\leq \sup_{\mathbf{x} \in \mathbb{C}^{m \cdot n}} \left\{ \left\| \lambda_1 \mathbb{M}_{\text{sb}} \mathbf{H}_{\text{TV}}(\mathbf{x}) \right\| + \left\| \lambda_2 \mathbb{M}_{\text{sb}} \mathbf{H}_{\text{W}}(\mathbf{x}) \right\| \right\} \\
&=: \overline{L} \;,
\end{aligned}
\quad (25)
$$

where the partial derivatives

$$
\begin{aligned}
\mathbf{H}_\iota(\mathbf{x}) &= \frac{\partial \mathbf{f}_\iota(\mathbf{x})}{\partial \mathbf{x}} \\
&= \frac{\boldsymbol{\Psi}_\iota^H \cdot \boldsymbol{\Psi}_\iota}{2 Q_\iota(\mathbf{x})} - \frac{\left(\boldsymbol{\Psi}_\iota^H \cdot \boldsymbol{\Psi}_\iota \cdot \mathbf{x} \right) \cdot \left(\boldsymbol{\Psi}_\iota^H \cdot \boldsymbol{\Psi}_\iota \cdot \mathbf{x} \right)^H}{4 Q_\iota^3(\mathbf{x})}
\end{aligned}
\quad (26)
$$

are well-defined and bounded for arbitrary complex arguments $\mathbf{x}$. Choosing suitably small values $0 \leq \lambda_1 \ll 1$ and $0 \leq \lambda_2 \ll 1$ (complying with the practical requirement that the consistency criterion $Q_1(\mathbf{x})$ defined in (2) has dominant influence on the optimal solution) completes the proof that $\overline{L} < 1$ and so that the iteration (20) converges. ∎

Remark 2. The advantage of the iteration, according to Theorem 2, is that it converges surely towards the globally optimal solution of the cost function (1). In contrast, this cannot be ensured for classical conjugate gradient approaches. Inappropriately chosen step size control procedures may prevent the desired convergence and probably lead to limit cycles during the iterative solution. Moreover, the admissible step sizes in gradient-based optimization techniques (unless chosen excessively small) depend on the actual values of the data $\mathbf{y}'$. Hence, the parallelization of such techniques is more challenging than the parallelization of fixed point iterations according to Eqn. (20).

Remark 3. The subdivision of $\mathbf{F}(\mathbf{y}', \mathbf{x}^{\langle \kappa \rangle})$ into terms that are either independent or dependent on $\mathbf{x}^{\langle \kappa \rangle}$ has the advantage that the term $\mathbb{M}_{\text{sb}} \cdot \boldsymbol{\mathcal{M}}_{\text{s}}^H \cdot \mathbf{y}'$, corresponding to the initialization $\mathbf{x}^{\langle 0 \rangle}$, only needs to be evaluated once, which reduces the computational effort.

3. Unscented transformation for stochastic uncertainty quantification

This section describes the application of the unscented transformation approach to the quantification of measurement uncertainty in MRI-based image reconstruction. It is then applied to further processing stages towards quantifying the influence of nonlinearities in phase angle reconstructions and resulting aggregations into an overall measurement result.

The algorithm consists of Steps U1–U5 listed in the following. It should be pointed out that either option (a) or option (b) of Step U5 is used depending on the information of interest in the application scenario at hand. The focus of option (a) is the numerical quantification of the accuracy of each reconstructed data point, while option (b) aims at determining the probability distribution of some aggregated information such as the overall flow rate through a specific cross section area in a pipe. For the sake of compliance and comparability with the results of John *et al.* (2020b) and Rauh *et al.* (2020), this paper is focused on option U5b.

U1 Determine the standard deviations σ_{Re} and σ_{Im} of the real and imaginary parts $\Re\{\mathbf{Y}\}$ and $\Im\{\mathbf{Y}\}$, respectively, over several repetitions of the identical measurement scenario.

U2 Initialize the expected value vector $\boldsymbol{\mu}$ as the average over the real and imaginary parts $\Re\{\mathbf{Y}\}$ and $\Im\{\mathbf{Y}\}$ of the measurement repetitions considered in U1.

U3 Treat the real and imaginary parts of all measured points in the vector $\mathbf{y}'$ as $2N'$ independent quantities and, hence, compute $4N'$ sigma points according to

$$\mathbf{y}'_{(i)} = \boldsymbol{\mu} + \tilde{\mathbf{y}}'_{(i)}, \quad i \in \{1, \ldots, 4N'\} \;, \quad (27)$$

where the increment vectors $\tilde{\mathbf{y}}'_{(i)}$ are defined by

$$\tilde{\mathbf{y}}'_{(i)} = \mathbf{e}_i \cdot \sqrt{2N'} \cdot \alpha \cdot \left(+\sigma_{\text{Re}} + \jmath \sigma_{\text{Im}} \right), \quad (28)$$
$$\tilde{\mathbf{y}}'_{(i+N')} = \mathbf{e}_i \cdot \sqrt{2N'} \cdot \alpha \cdot \left(+\sigma_{\text{Re}} - \jmath \sigma_{\text{Im}} \right), \quad (29)$$
$$\tilde{\mathbf{y}}'_{(i+2N')} = \mathbf{e}_i \cdot \sqrt{2N'} \cdot \alpha \cdot \left(-\sigma_{\text{Re}} + \jmath \sigma_{\text{Im}} \right), \quad (30)$$
$$\tilde{\mathbf{y}}'_{(i+3N')} = \mathbf{e}_i \cdot \sqrt{2N'} \cdot \alpha \cdot \left(-\sigma_{\text{Re}} - \jmath \sigma_{\text{Im}} \right), \quad (31)$$

with $\mathbf{e}_i$ being the i-th unit vector[4] of dimension N' and $i \in \{1, \ldots, N'\}$. Here, $0 < \alpha \leq 1$ is a user-defined scaling parameter, determining the distance of the sigma points from the expected value $\boldsymbol{\mu}$ of the measurements. Its optimal choice is a matter of ongoing research.

U4 Perform the iterative image reconstruction of Theorem 2 for each sigma point in the range $i \in$

---

[4]Defined according to Eqn. (10).

$\{1, \ldots, 4N'\}$ according to

$$\mathbf{x}_{(i)}^{\langle \kappa+1 \rangle} = \mathbf{F}\big(\mathbf{y}'_{(i)}, \mathbf{x}_{(i)}^{\langle \kappa \rangle}\big), \tag{32}$$

and denote by $\mathbf{x}_{(i)}$ the result of the iteration.

U5a Determine the expected value over all sigma points $\mathbf{x}_{(i)}$ propagated through the iteration formula $\mathbf{F}(\cdot)$ as well as the respective covariance according to

$$\bar{\mathbf{x}} = \frac{1}{4N'} \sum_{i=1}^{4N'} \mathbf{x}_{(i)} \tag{33}$$

and

$$\mathbf{C}_x = \frac{1}{4N'} \sum_{i=1}^{4N'} \big(\mathbf{x}_{(i)} - \bar{\mathbf{x}}\big)\big(\mathbf{x}_{(i)} - \bar{\mathbf{x}}\big)^H \tag{34}$$

as the uncertainty model of the image reconstruction.

U5b Compute the value $\boldsymbol{\varphi}_{(i)}$ of the phase angle for all sigma points (i.e., the `atan2` function applied to each entry of $\mathbf{x}_{(i)}$) which contains the measured value, e.g., the fluid velocity $\mathbf{v}_{(i)}$ as described in the following section. Average over all $\mathbf{v}_{(i)}$ (resp., $\boldsymbol{\varphi}_{(i)}$) to obtain $\bar{\mathbf{v}}$ (resp., $\bar{\boldsymbol{\varphi}}$) and determine their scalar variance to describe a Gaussian approximation of the reconstructed mean value on the basis of the unscented transformation. In addition, extract the histogram over all $\mathbf{v}_{(i)}$ to estimate the effects of nonlinearities in the reconstruction in terms of deviations of the shape (skewness and kurtosis) from that of an idealized Gaussian PDF.

Remark 4. For a computationally efficient MATLAB implementation, it is reasonable to avoid the evaluation of the individual sigma points $i \in \{1, \ldots, 4N'\}$ in a `for` loop. Instead, all vectors $\mathbf{y}'_{(i)}$ should be collected as columns of a matrix of dimension $N' \times (4N')$ on which the iteration $\mathbf{F}(\cdot)$ is applied. In such a way, also a massively parallelized implementation on NVIDIA GPUs becomes possible by converting the data $\mathbf{y}'_{(i)}$ (prior to the iteration) into the datatype `gpuArray` provided by the PARALLEL COMPUTING TOOLBOX.

4. Experimental validation of the unscented transformation technique for uncertainty quantification in MRI

To validate the presented unscented transformation approach, the phase data for a velocity-sensitive MRI measurement of the fluid flow in a circular-shaped pipe acquired for a specific cross-section as published by John *et al*. (2020b) are employed. These phase data are converted to the fluid velocity via
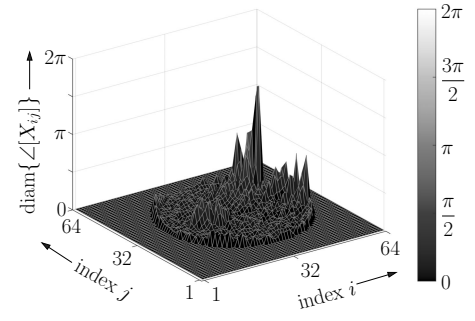
$$\bar{\mathbf{v}} = \bar{\boldsymbol{\varphi}} \cdot \frac{V_{\mathrm{enc}}}{\pi}, \tag{35}$$
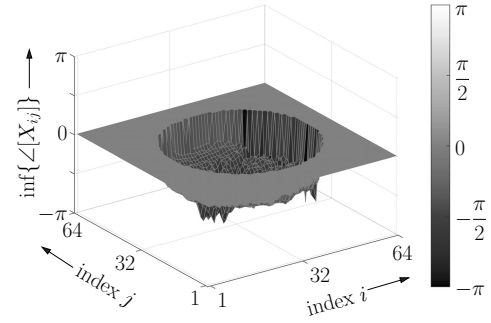
(a) lower estimate $\min\{\angle[\mathbf{X}]\}$.
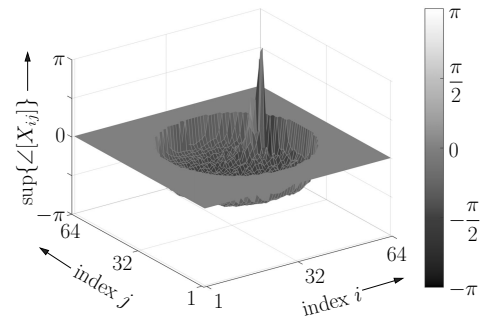
(b) upper estimate $\max\{\angle[\mathbf{X}]\}$.

(c) uncertainty range $\mathrm{diam}\{\angle[\mathbf{X}]\}$.

Fig. 1. Predicted uncertainty in the reconstruction of the phase angle $\angle[\mathbf{X}]$ for the sampling percentage 60%.

where V_{enc} denotes the velocity sensitivity value. As a global measure, the velocity data points are integrated over the cross-section which yields the flow rate

$$Q = \sum_{i=1}^{m \cdot n} v_i \cdot M_i \cdot \mathrm{d}A, \tag{36}$$

where $\mathrm{d}A$ is the area of each data point and $\mathbf{M} = \mathrm{col}(\mathbf{M}_{\mathrm{b}})$ is the binary mask defining the fluid filled cross-section in the image. In addition, also the parameter settings $\lambda_1 = 10^{-3}$, $\lambda_2 = 0$, $\lambda_3 = 0.01$, and $\mu_{\mathrm{TV}} = 10^{-6}$ were employed. From a practical point of view, the suitability of these parameters can be confirmed
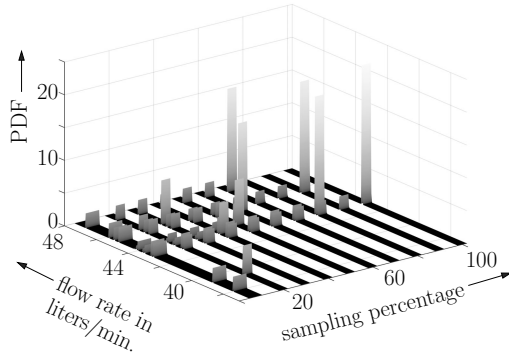
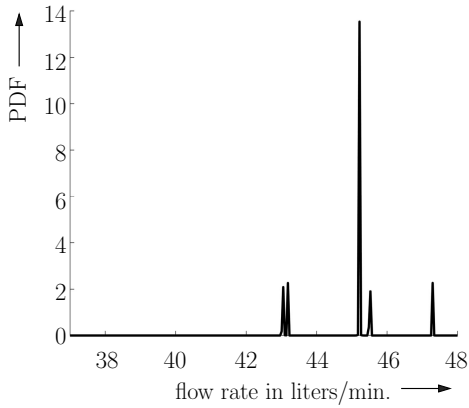Fig. 2. PDFs of the flow rate for all sampling percentages $\mathcal{S}$.

Fig. 3. Detailed view of the estimated PDF of the reconstructed flow rate for 60% sampling.

by comparing the result of the flow rate reconstruction with a flow rate assessment using a diverse sensor. For all results summarized in the following, the scaling parameter introduced in (28)–(31) is set to $\alpha = 1$ in accordance with the original work of Julier *et al.* (2000). Then, for the range of sampling percentages $\mathcal{S} = \{10\%, 20\%, \ldots, 100\%\}$ of the k-space, the phase distributions of the complex-valued images $\mathbf{X}_{(i)}$ were reconstructed for each sigma point $\mathbf{y}'_{(i)}, i \in \{1, \ldots, 4N'\}$.

Computing the minimum and maximum phase angles over the respective matrix entries of all reconstruction results $\mathbf{X}_{(i)}$, the prediction results visualized in Fig. 1 are obtained. Exemplarily, Fig. 1 makes use of the sampling percentage 60%. The uncertainty range in Fig. 1(c) corresponds to the point-wise difference of the maxima and minima in Figs. 1(b) and 1(a) and confirms the uncertainty distribution already forecasted by John *et al.* (2020b) with the help of a non-probabilistic interval approach.

Considering further the flow rate Q as defined in (36) for the cross section under investigation, and computing normalized histograms over all $i \in \{1, \ldots, 4N'\}$ for each sampling percentage as an approximation to the PDF in

terms of the frequency distribution of the reconstructed flow rate, the result in Fig. 2 is obtained. Here, it becomes obvious that it is only in the case of a fully sampled data set (100%) that the resulting PDF becomes unimodal and close to a normal distribution.[5] In all other cases, the PDF characterizing the uncertainty in the reconstructed flow rate exhibits a multi-modal shape. Exemplarily, this is shown in Fig. 3 again for the case of a 60% sampling.

The multi-modality of the PDFs in Figs. 2 and 3 seems to be related to the staircase effect described by Zhou *et al.* (2020). Hence, future research will be directed towards analyzing not only the influence of replacing the first-order approximation of the sparsity enforcing TV operator by higher-order alternatives, but also the introduction of further penalty terms in the cost function (1) that reduce the sensitivity of the reconstruction with respect to randomly leaving out further measured data points as a kind of artificial undersampling. Note that ideas from other image processing techniques which gradually try to gather further data points for enhancing the result of reconstruction contradict the general goal of undersampling where the speed-up of MRI data acquisition is crucially achieved by minimizing the amount of gathered data.

The uncertainty in the reconstructed flow rate Q increases continuously when the sampling percentage in the k-space data is gradually reduced. Figure 4 depicts the expected values of an approximating Gaussian PDF resulting from the unscented transformation by means of black bullets, the 1-standard deviation ranges by black error bars and the range over all reconstruction results for $i \in \{1, \ldots, 4N'\}$ in terms of gray boxes. Comparing these results with the corresponding PDFs in Fig. 2, it can be noticed that the reconstruction results are quite insensitive against the sampling percentage, except for the two lowest values.

As already stated in Remark 2, the proposed iterative solution technique is well suited for parallelization as well as easily portable to modern GPU architectures. The comparison according to Fig. 5 is based on a MATLAB R2019b implementation on Windows 10, 64-bit, where two Intel Xeon E5-2609v2 CPUs (@2.50GHz) with 64 GB RAM and an NVIDIA Tesla K20c GPU (@0.7GHz, 5GB memory) are available. Using comparable stopping criteria for a gradient-based optimization (cf. John *et al.*, 2020b), as well as for the novel procedure, it is obvious that, even for a single data set, the new iteration outperforms the classical gradient-based implementation by a factor of more than 2.5 concerning its speed.

Accounting for the matrix-vector implementation of (20), the GPU version is faster by a factor of

---

[5]Note that the reconstruction of the image $\mathbf{X}$ is normally distributed for fully sampled data sets. Then, deviations from a Gaussian PDF are caused by the arc-tangent function in the phase reconstruction.
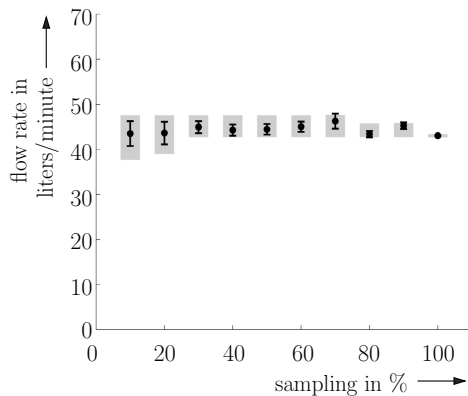
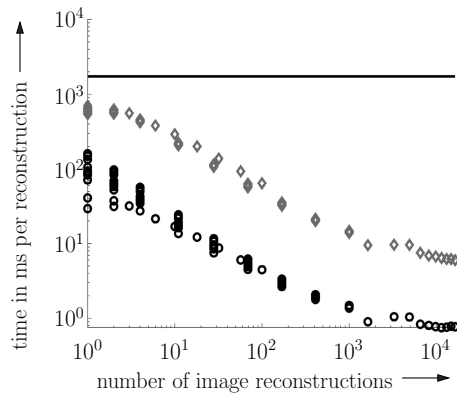Fig. 4. Reconstructed flow rate Q for all sampling percentages $\mathcal{S}$.

Fig. 5. Computing time per image reconstruction for a non-parallelized CPU implementation of a conjugate gradient approach (solid line), a vectorized CPU implementation of Theorem 2 ($\lozenge$), and a GPU-based counterpart ($\circ$).

approximately 10 up to the fully sampled data set with $16{,}384$ parallel evaluations of the image reconstruction, where each data set consists of 4096 pixels. This image size also becomes a limiting factor due to memory restrictions of the GPU. Note that the vertical variabilities of the data points in Fig. 5 result from various sampling percentages where choosing smaller ones typically accelerates the reconstruction.

5. Conclusions and future work

In this paper, an unscented transformation technique for the stochastic uncertainty quantification of MRI measurements was derived and successfully validated. Future work will aim at the derivation of more detailed confidence intervals based on this research to refine the solution already investigated by John *et al.* (2020b) by means of interval analysis. Related approaches for such a kind of uncertainty quantification can be found with the help of the so-called type 2 interval arithmetic (Piegat

and Dobryakova, 2020), where the interval boundaries themselves turn into uncertain quantities.

Moreover, the influence of the sigma point scaling parameter α will be investigated for the case of more complex fluidic systems. Currently, numerical investigations have shown that variations of this parameter only have very little influence on the reconstruction results. Finally, reasons for the arising multi-modalities in the reconstructed PDFs, their correlation with specific frequencies in the measured data set, and strategies for their avoidance by enhanced undersampling and image reconstruction techniques will be taken into consideration.

References

Bouboulis, P. (2010). Wirtinger's calculus in general Hilbert spaces, *arXiv*:1005.5170.

Bruschewski, M., Freudenhammer, D., Buchenberg, W.B., Schiffer, H.-P. and Grundmann, S. (2016). Estimation of the measurement uncertainty in magnetic resonance velocimetry based on statistical models, *Experiments in Fluids* **57**(5): 83.

Bruschewski, M., Kolkmann, H., John, K. and Grundmann, S. (2019). Phase-contrast single-point imaging with synchronized encoding: A more reliable technique for in vitro flow quantification, *Magnetic Resonance in Medicine* **81**(5): 2937–2946.

Datta, A., Kaur, A., Lauer, T. and Chabbouh, S. (2019). Exploiting multi-core and many-core parallelism for subspace clustering, *International Journal of Applied Mathematics and Computer Science* **29**(1): 81–91, DOI: 10.2478/amcs-2019-0006.

Elkins, C.J. and Alley, M.T. (2007). Magnetic resonance velocimetry: Applications of magnetic resonance imaging in the measurement of fluid motion, *Experiments in Fluids* **43**(6): 823–858.

Gentleman, W.M. (1968). Matrix multiplication and fast Fourier transforms, *Bell System Technical Journal* **47**(6): 1099–1103.

Holland, D.J., Malioutov, D.M., Blake, A., Sederman, A.J. and Gladden, L.F. (2010). Reducing data acquisition times in phase-encoded velocity imaging using compressed sensing, *Journal of Magnetic Resonance* **203**(2): 236–246.

Hörmander, L. (1990). *An Introduction to Complex Analysis in Several Variables*, 3rd Edn, North-Holland, Amsterdam.

John, K., Jahangir, S., Gawandalkar, U., Hogendoorn, W., Poelma, C., Grundmann, S. and Bruschewski, M. (2020a). Magnetic resonance velocimetry in high-speed turbulent flows: Sources of measurement errors and a new approach for higher accuracy, *Experiments in Fluids: Experimental Methods and Their Applications to Fluid Flow* **61**(2): 27.

John, K., Rauh, A., Bruschewski, M. and Grundmann, S. (2020b). Towards analyzing the influence of measurement errors in magnetic resonance imaging of fluid flows—Development of an interval-based iteration approach, *Acta Cybernetica* **24**(3): 343–372.

Julier, S., Uhlmann, J. and Durrant-Whyte, H. (2000). A new approach for the nonlinear transformation of means and covariances in filters and estimators, *IEEE Transactions on Automatic Control* **45**(3): 477–482.

Kostin, G.V., Saurin, V.V., Aschemann, H. and Rauh, A. (2014). Integrodifferential approaches to frequency analysis and control design for compressible fluid flow in a pipeline element, *Mathematical and Computer Modelling of Dynamical Systems* **20**(5): 504–527.

Măceş, D. and Stadtherr, M. (2013). Computing fuzzy trajectories for nonlinear dynamic systems, *Computers & Chemical Engineering* **52**: 10–25.

Niebergall, A., Zhang, S., Kunay, E., Keydana, G., Job, M., Uecker, M. and Frahm, J. (2013). Real-time MRI of speaking at a resolution of 33 ms: Undersampled radial FLASH with nonlinear inverse reconstruction, *Magnetic Resonance in Medicine* **69**(2): 477–485.

Piegat, A. and Dobryakova, L. (2020). A decomposition approach to type 2 interval arithmetic, *International Journal of Applied Mathematics and Computer Science* **30**(1): 185–201, DOI: 10.34768/amcs-2020-0015.

Proakis, J.G. and Manolakis, D.G. (1996). *Digital Signal Processing: Principles, Algorithms, and Applications*, 3rd Edn, Prentice-Hall, Upper Saddle River.

Rao, K.R. and Yip, P.C. (2000). *The Transform and Data Compression Handbook*, CRC Press, Boca Raton.

Rauh, A., Dittrich, C., Senkel, L. and Aschemann, H. (2011). Sensitivity analysis for the design of robust nonlinear control strategies for energy-efficient pressure boosting systems in water supply, *Proceedings of the 20th International Symposium on Industrial Electronics, ISIE 2011, Gdańsk, Poland*, pp.1353–1358.

Rauh, A., John, K., Bruschewski, M. and Grundmann, S. (2020). Comparison of two different interval techniques for analyzing the influence of measurement uncertainty in compressed sensing for magnet resonance imaging, *Proceedings of the 18th European Control Conference, ECC 2020, St. Petersburg, Russia*, pp. 1865–1870.

Tamir, J., Ong, F., Cheng, J., Uecker, M. and Lustig, M. (2016). Generalized magnetic resonance image reconstruction using the Berkeley Advanced Reconstruction Toolbox, *ISMRM Workshop on Data Sampling and Image Reconstruction, Sedona, USA*, `http://wwwuser.gwdg.de/~muecker1/sedona16-bart.pdf`.

Theilheimer, F. (1969). A matrix version of the fast Fourier transform, *IEEE Transactions on Audio and Electroacoustics* **17**(2): 158–161.

Uhlmann, J. (2021). First-hand: The unscented transform, `https://ethw.org/First-Hand:The_Unscented_Transform`.

Weinmann, A. (1991). *Uncertain Models and Robust Control*, Springer, Vienna.

Zhao, F. (2014). *Methods for MRI RF Pulse Design and Image Reconstruction*, PhD thesis, University of Michigan, Ann Arbor.

Zhao, F., Noll, D., Nielsen, J.-F. and Fessler, J. (2012). Separate magnitude and phase regularization via compressed sensing, *IEEE Transactions on Medical Imaging* **31**(9): 1713–1723.

Zhou, B., Yang, Y.-F. and Hu, B.-X. (2020). A second-order TV-based coupling model and an ADMM algorithm for MR image reconstruction, *International Journal of Applied Mathematics and Computer Science* **30**(1): 113–122, DOI: 10.34768/amcs-2020-0009.

Andreas Rauh was born in Munich, Germany, in 1977. He received his diploma degree in electrical engineering and information technology from Technische Universität München, Germany, in 2001, his PhD degree (Dr.-Ing.) from the University of Ulm, Germany, in 2008, and his habilitation (Dr.-Ing. habil.) in measurement technology and automatic control from the University of Rostock, Germany, in 2017. He has published more than 170 articles and chapters in edited books, international conferences and peer-reviewed journals with the focus on modeling, control, as well as state and parameter estimation for systems with stochastic and set-valued uncertainty. Since 2008 he has been a member of the IEEE 1788 Working Group for the Standardization of Interval Arithmetic.

Kristine John was born in Rostock, Germany, in 1991. She received her Master's degree in mechanical engineering from the University of Rostock in 2017. Since then, she has been a PhD student with the Institute of Fluid Mechanics there. Her research focuses on magnetic resonance velocimetry in technical flow systems.

Carolin Wüstenhagen was born in Parchim, Germany, in 1991. She received her Master's degree in technomathematics from the University of Rostock, Germany, in 2015. Since then, she has been working there as a research associate in biomedical engineering and, currently, in the field of magnetic resonance velocimetry in technical flow systems at the Institute of Fluid Mechanics.

Martin Bruschewski was born in Langen, Germany, in 1986. He received his Bachelor's and Master's degrees in mechanical engineering from Technische Universität Darmstadt in 2009 and 2011, and his PhD degree (Dr.-Ing.) in 2016. Since 2016 he has been working at the Institute of Fluid Mechanics of the University of Rostock, where he heads the team and the laboratory for magnetic resonance imaging. He has published more than 30 articles in international conferences and peer-reviewed journals with a focus on experimental fluid mechanics, magnetic resonance imaging, measurement science, gas turbine cooling, and nuclear reactor safety research.

Sven Grundmann was born in Cologne, Germany, in 1975. He received his diploma degree in mechanical engineering in 2003, his PhD degree (Dr.-Ing.) in 2008, and his habilitation (Dr.-Ing. habil.) in fluid mechanics in 2014, all from Technische Universität Darmstadt, Germany. He has published more than 150 articles in international conferences and peer-reviewed journals with the focus on flow control, fluid mechanics and magnetic resonance velocimetry. Since 2019 he has been a member of the Grants Committee and the Senate Committee on Research Training Groups of the German Research Association DFG.